nature communications

Article

https://doi.org/10.1038/s41467-025-59255-7

Structure and transport mechanism of human riboflavin transporters

Received: 26 March 2025

Accepted: 11 April 2025

Published online: 01 May 2025

Check for updates

Ke Wang[1,2,7], Huiwen Chen[1,2,7], Lili Cheng[3,7], Jun Zhao[4,7], Bo Huang[5,7], Di Wu[2,6], Xin He[3], Yumeng Zhou[3], Yaxuan Yuan[3], Feng Zhou[5], Juquan Jiang[1] ✉, Ligong Chen[3] ✉ & Daohua Jiang[2,6] ✉

Riboflavin (vitamin B2) is the precursor of flavin mononucleotide (FMN) and flavin adenine dinucleotide (FAD), which act as key cofactors of many enzymes, thus has essential roles in cell growth and functions. Animals cannot synthesize riboflavin in situ, the intake, distribution and metabolism of which are mediated by three riboflavin transporters (RFVT1-3). Many mutations in RFVTs cause severe consequences. How RFVTs recognize and transport riboflavin remains largely unknown. Here we describe the cryo-electron microscopy structures of human RFVT2 and RFVT3 in complex with riboflavin in outward-occluded and inward-open states, respectively. Riboflavin is recognized by a conserved binding pocket in the central cavity of RFVTs, whereas two acidic residues in RFVT3 determine its pH-dependent activity. By combining the structural, computational and functional analyses, this study demonstrates the structural basis of riboflavin recognition and provides a structural framework for the mechanistic comprehension of riboflavin recognition, transport, and pathology in human RFVTs.

Cells take up riboflavin (also known as vitamin B2) and convert it into its active forms flavin mononucleotide (FMN) and flavin adenine dinucleotide (FAD), which function as essential cofactors for various flavoenzymes that have crucial roles in cellular metabolism, including energy generation, biomacromolecule synthesis and xenobiotic disposition[1–3] (Fig. 1a). Because humans are unable to synthesize riboflavin, the European Food Safety Authority (EFSA) recommends that adults need to intake at least 1 mg of riboflavin daily from the diet to maintain riboflavin homeostasis[4]. To exert these indispensable functions, riboflavin must be transported across the cell membrane. Three riboflavin transporters, RFVT1-3 (encoded by *SLC52A1-3*)[5–7], mediate the absorption, distribution and reabsorption of riboflavin, playing a vital role in riboflavin homeostasis[8–10]. RFVTs have a specific tissue distribution. RFVT1 is expressed in the placenta and small intestine[5,6], and RFVT3 is predominantly expressed in the testis, small intestine, kidney, and placenta[7,11], whereas RFVT2 is ubiquitously distributed and is highly expressed in the brain[6,12]. Altered riboflavin homeostasis and dysfunction of RFVTs can cause pathological consequences, such as multiple acyl-CoA dehydrogenase deficiency (MADD)[13,14] and Brown-Vialetto-van Laere syndrome[9,10,15–17]. Additionally, RFVT1-3 were suggested to be overexpressed in many types of tumors, including melanoma and brain cancer[18], colorectal cancer[19] and esophageal cancer[20]. Riboflavin-conjugated anticancer drug delivery methods have been emerging[18,21]. Despite the physiological and potential pharmacological importance of RFVTs, the lack of accurate structural information hinders the mechanistic comprehension of RFVT functions and further investigation of RFVTs as a potential anticancer target.

[1]Department of Microbiology and Biotechnology, College of Life Sciences, Northeast Agricultural University, Harbin, China. [2]Beijing National Laboratory for Condensed Matter Physics and Institute of Physics, Chinese Academy of Sciences, Beijing, China. [3]School of Pharmaceutical Sciences, Beijing Frontier Research Center for Biological Structure, Tsinghua University, Beijing, China. [4]Peking University Institute of Advanced Agricultural Sciences, Shandong Laboratory of Advanced Agricultural Sciences at Weifang, Weifang, Shandong, China. [5]Beijing StoneWise Technology Co Ltd., Beijing, China. [6]School of Physical Sciences, University of Chinese Academy of Sciences, Beijing, China. [7]These authors contributed equally: Ke Wang, Huiwen Chen, Lili Cheng, Jun Zhao, Bo Huang. ✉e-mail: jjqdainty@163.com; ligongchen@tsinghua.edu.cn; jiangdh@iphy.ac.cn

https://doi.org/10.1038/s41467-025-59255-7

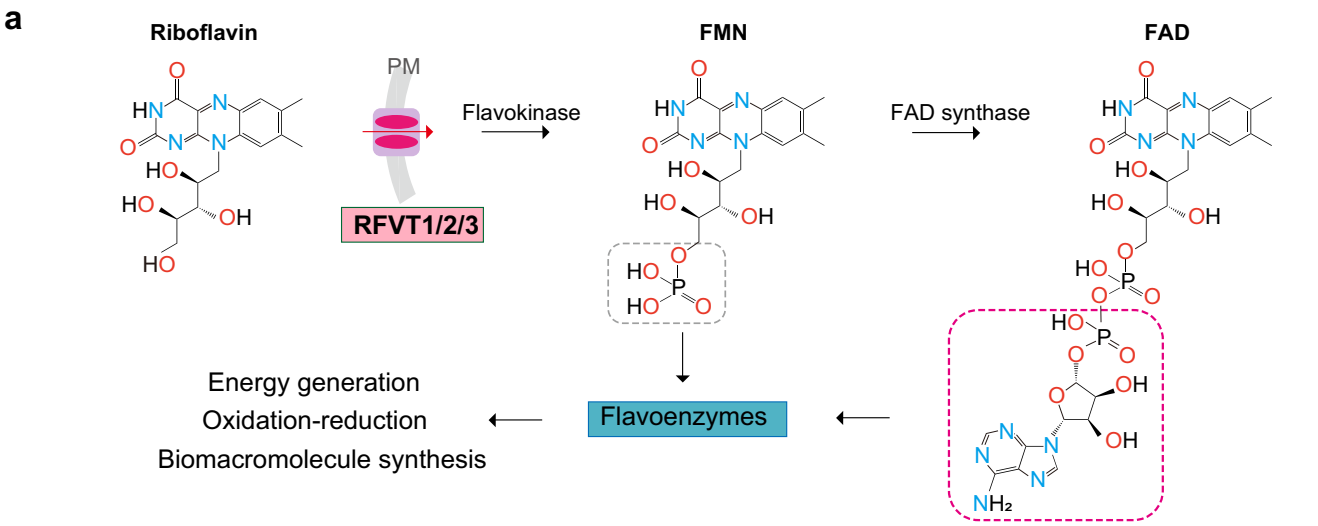

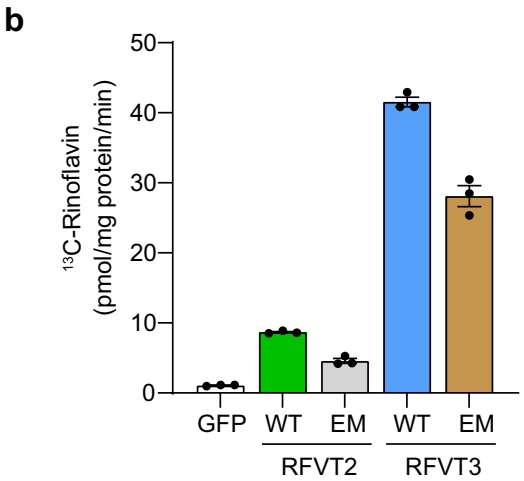

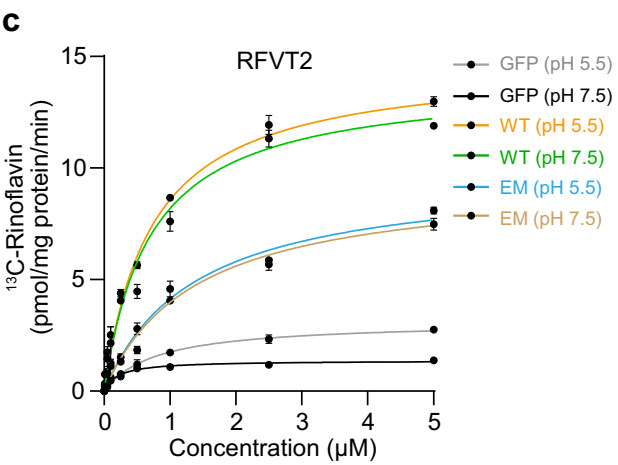

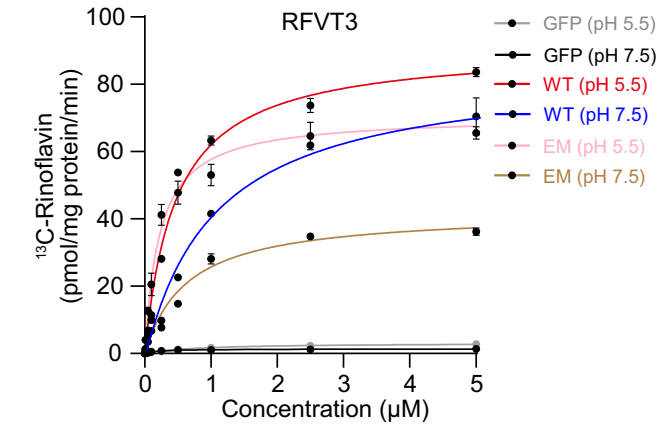

e

	Vmax (pmol/mg protein/min)	Km (μM)
RFVT2-WT (pH 5.5)	14.77 ± 0.59	0.72 ± 0.07
RFVT2-WT (pH 7.5)	13.93 ± 0.55	0.70 ± 0.08
RFVT2-EM (pH 5.5)	9.76 ± 0.50	1.36 ± 0.17
RFVT2-EM (pH 7.5)	9.46 ± 0.49	1.38 ± 0.17
RFVT3-WT (pH 5.5)	91.12 ± 2.11	0.47 ± 0.03
RFVT3-WT (pH 7.5)	83.12 ± 2.31	1.08 ± 0.09
RFVT3-EM (pH 5.5)	70.60 ± 2.40	0.22 ± 0.03
RFVT3-EM (pH 7.5)	42.12 ± 1.83	0.64 ± 0.08

Fig. 1 | Functional characterization of RFVT2 and RFVT3. a The schematic diagram for the metabolic pathway and function of riboflavin. PM plasma membrane, FMN flavin mononucleotide, FAD flavin adenine dinucleotide. **b** Riboflavin uptake by wild-type (WT) and EM forms of RFVT2 and RFVT3. Cells were subjected to 1 μM [13C]riboflavin for 1 min. Cells expressing GFP served as controls. Data are presented as mean ± s.e.m.; $n = 3$ independent replicates. **c**, **d** Concentration-dependent uptake of [^{13}C]riboflavin by HEK293T cells transfected with RFVT2 (**c**) and RFVT3 (**d**). Cells expressing GFP served as controls. Data are presented as mean ± s.e.m.; $n = 3$ independent replicates. **e** The riboflavin uptake kinetics of WT and EM forms of RFVT2 and RFVT3. Source data are provided as a Source Data file.

RFVTs belong to the solute carrier 52 (SLC52) family[10], which exhibit little similarity to other riboflavin transporters in bacteria and fungi[22–24]. While RFVT1 (formerly known as RFT1) and RFVT2 (formerly known as RFT3) are highly conserved and share a high sequence identity of ~85%, they are less similar to RFVT3 (formerly known as RFT2), with a sequence identity of ~41%[10]. Experimental evidence has indicated that the three RFVTs exhibit a similar riboflavin specificity and Na^+- or Cl^--independent transport activities[5–7,25]; however, only

RFVT3 displays low pH-enhanced activity and has a greater capacity than RFVT1 and RFVT2[6,7,25]. The precise mechanisms underlying riboflavin recognition and transport in RFVTs and the low pH-enhanced activity in RFVT3 have not been elucidated.

In this study, we determined the cryo-electron microscopy (cryo-EM) structures of human RFVT2 and RFVT3 in complex with riboflavin, elucidating the principles of riboflavin recognition and transport in human RFVTs. Structural comparisons of RFVT2 and RFVT3 revealed a conserved riboflavin binding site. Augmented with mutagenesis and proteoliposome transport assays, our work defines that two acidic residues, D119 and E145, which are not conserved in RFVT1 and RFVT2, determine the pH-dependent activity of RFVT3.

Results

Functional characteristics of RFVT2 and RFVT3

We first assayed the transport activity of human wild-type (WT) RFVT2 and RFVT3 expressed in HEK293T cells. Both RFVT2 and RFVT3 expressing cells exhibited robust accumulation of [^{13}C]riboflavin using quantitative mass spectrometry analysis, which are ~8- and ~38-fold of the basal activity of HEK293T cells expressing green fluorescent protein (GFP) alone, respectively (Fig. 1b). We next investigated the concentration-dependent uptake of [^{13}C]riboflavin by RFVT2 and RFVT3 at pH 7.5, yielding apparent *K*m values of RFVT2 and RFVT3 for riboflavin at 0.7 μM and 1.1 μM, respectively; however, the *V*max value of RFVT3 (83.1 pmol/mg protein/min) is ~6-fold of that of RFVT2 (13.9 pmol/mg protein/min) (Fig. 1c–e). We further examined pH-dependent uptake of RFVT2 and RFVT3, which clearly shows that different pH values have no effect on RFVT2 kinetics, while a low pH of 5.5 significantly enhances RFVT3 activity with increased *V*max and decreased *K*m (Fig. 1c–e). These functional results demonstrate similar riboflavin specificity but distinct pH dependency of RFVT2 and RFVT3, which are consistent with the findings of previous studies[6,7,26].

Human RFVTs are small membrane proteins of ~50 kDa in size, and solving their cryo-EM structures is very challenging due to the small size and lacking discernible soluble domain. To facilitate structure determination, we employed GFP and a nanobody specific to GFP as a fiducial marker[27] and fused GFP to the N-terminus and the nanobody between E228 and P262 of RFVT2 and between P267 and A293 of RFVT3 (Supplementary Fig. 1a, b), which we termed RFVT2^{EM} and RFVT3^{EM}, respectively. We examined the functional characteristics of the EM constructs. RFVT2^{EM} displays similar *K*m value and pH-independent activity to those of RFVT2^{WT}, although its *V*max is reduced to ~65% of that of RFVT2^{WT}; RFVT3^{EM} exhibits low pH enhanced activity and decreased *K*m and *V*max values in comparison to those of RFVT3^{WT} (Fig. 1c–e). These results confirm that both the EM constructs retain the key functional characteristics of their respective WT forms and thus are suitable for structural study.

Cryo-EM structures of RFVT2 and RFVT3

To determine the structural basis of riboflavin recognition in RFVTs, we purified RFVT2^{EM} and RFVT3^{EM} samples in the presence of riboflavin and performed cryo-EM analysis of the samples (Supplementary Figs. 1–3). During EM data processing, we noticed that the density for GFP-nanobody is poor compared to those of RFVTs, and the linkers between them are invisible, further indicating that the fiducial marker is sufficient for particle alignment but does not constrain RFVT function (Supplementary Figs. 2b and 3b). Using a focused mask, the final EM maps of RFVT2^{EM} and RFVT3^{EM} were determined at nominal resolution of 3.0 Å and 3.3 Å, respectively (Supplementary Figs. 2, 3 and Supplementary Table 1). These high-quality density maps permitted accurate model building of the RFVTs and the assignment of riboflavin (Fig. 2a–d, Supplementary Figs. 2e–g and 3e–g). Specifically, the structure of RFVT2 displays a narrow central cavity that opens to the extracellular space, where the bound riboflavin is partially embedded, suggesting that RFVT2 was captured in an outward-occluded state (Fig. 2e). By contrast, RFVT3 adopts an inward- open conformation with the bound riboflavin exposing to the cytosol (Fig. 2f). These RFVT structures represent two key states in the transport cycle of RFVTs.

Both RFVT2 and RFVT3 consist of 11 transmembrane helices (TM1-11), of which TM1-6 form the N-domain and TM7-11 form the C-domain (Fig. 2c–f), exhibiting an asymmetric 6 + 5 topology. Although adopting different conformations, structural alignments revealed that the N-domains and the C-domains of RFVT2 and RFVT3 are highly similar, as indicated by the root mean square deviation (r.m.s.d.) values of 1.3 Å over 173 Cα atoms between the N-domains and of 0.9 Å over 156 Cα atoms between the C-domains (Supplementary Fig. 4a). For each of the RFVTs, the N-domain can be well superimposed with the C-domain. Additionally, TM1-3 resembles TM4-6, and TM7-9 shows similarity to TM10-11, despite the lack of a third TM helix in this repeat (Supplementary Fig. 4b–d). These interdomain pseudo-symmetries are reminiscent of the structural features of the major facilitator superfamily (MFS) transporters[28,29]. Interestingly, the RFVTs exhibit marked similarity to the equilibrative nucleoside transporter 1 (ENT1)[30,31] of the SLC29 family (Supplementary Fig. 4e–h), members of which also possess this atypical 6 + 5 topology and are classified as MFS-like transporters[32,33]. However, RFVTs display distinguishable structural features. First, the unwound TM1 is broken into TM1a and TM1b by a conserved “GMGSW” motif, and the twisted TM7 contains a turn of π-helix in the middle, suggesting that TM1 and TM7 are gating helices in which these hinge regions confer flexibility for local conformational changes upon riboflavin binding (Supplementary Fig. 4i). Second, two short antiparallel β-sheets were observed between TM3 and TM4. And lastly, the C-terminal loop folds back onto the interface between the N- and C-domains (Supplementary Fig. 4j).

Riboflavin recognition by RFVTs

In both RFVTs, TM1, TM4 and TM5 from the N-domain and TM7, TM10 and TM11 from the C-domain enclosed a highly-hydrophilic central cavity, inside which unambiguous EM densities were observed belonging to the bound riboflavin molecules (Fig. 3a, d and Supplementary Figs. 2f and 3f). The bound riboflavin is vertically placed in the cavity and forms extensive interactions with surrounding residues (Fig. 3a–f). In the outward-occluded RFVT2, riboflavin is partly covered by W31 from TM1. The flat isoalloxazine ring is sandwiched by W24 on TM1 and N291 on TM7 (Fig. 3b and Supplementary Fig. 4i). The mutations W24A, W24F, W31A and N291A greatly impaired [^{13}C]riboflavin uptake by RFVT2; however, W31F retained ~50% activity of RFVT2^{WT} (Fig. 3g), suggesting a critical role of W24 and N291 in riboflavin recognition and an important role of W31 as a lid. This three-ring moiety also forms hydrophobic interactions with V27 and W31 on TM1, V55 on TM2 and P295 on TM7 and multiple hydrogen bond interactions with W24, N129, N291, K390 and Q413. Additionally, the hydrophilic ribityl tail engages in hydrogen bond interactions with N28, backbone carbonyl oxygen atom of Q151, and N291. In agreement with these specific interactions, the N28A, K390Q, Q413N and Q413A mutations strongly impaired riboflavin uptake, whereas K390A and K390R kept ~40% activity, N129A and Q151A retained ~50% activity (Fig. 3g). Biochemical and plasma membrane expression assays demonstrated that most of these mutants behave similarly to the WT form, whereas the K390Q mutant exhibits a broad fluorescence-detection size-exclusion chromatography (fSEC) profile and a pattern of non-plasma membrane localization (Supplementary Fig. 1e–m), indicating that K390Q may disturb protein stability and tracking, which contribute to its completely abolished activity (Fig. 3g). These findings suggest that the isoalloxazine ring is the main determinant for riboflavin recognition, which is in line with the fact that lumiflavin, a derivative of riboflavin lacking the ribityl moiety, can completely inhibit riboflavin transport in RFVTs in a competitive manner[6,25]. Moreover, FMN can exert a greater inhibitory effect on riboflavin

https://doi.org/10.1038/s41467-025-59255-7

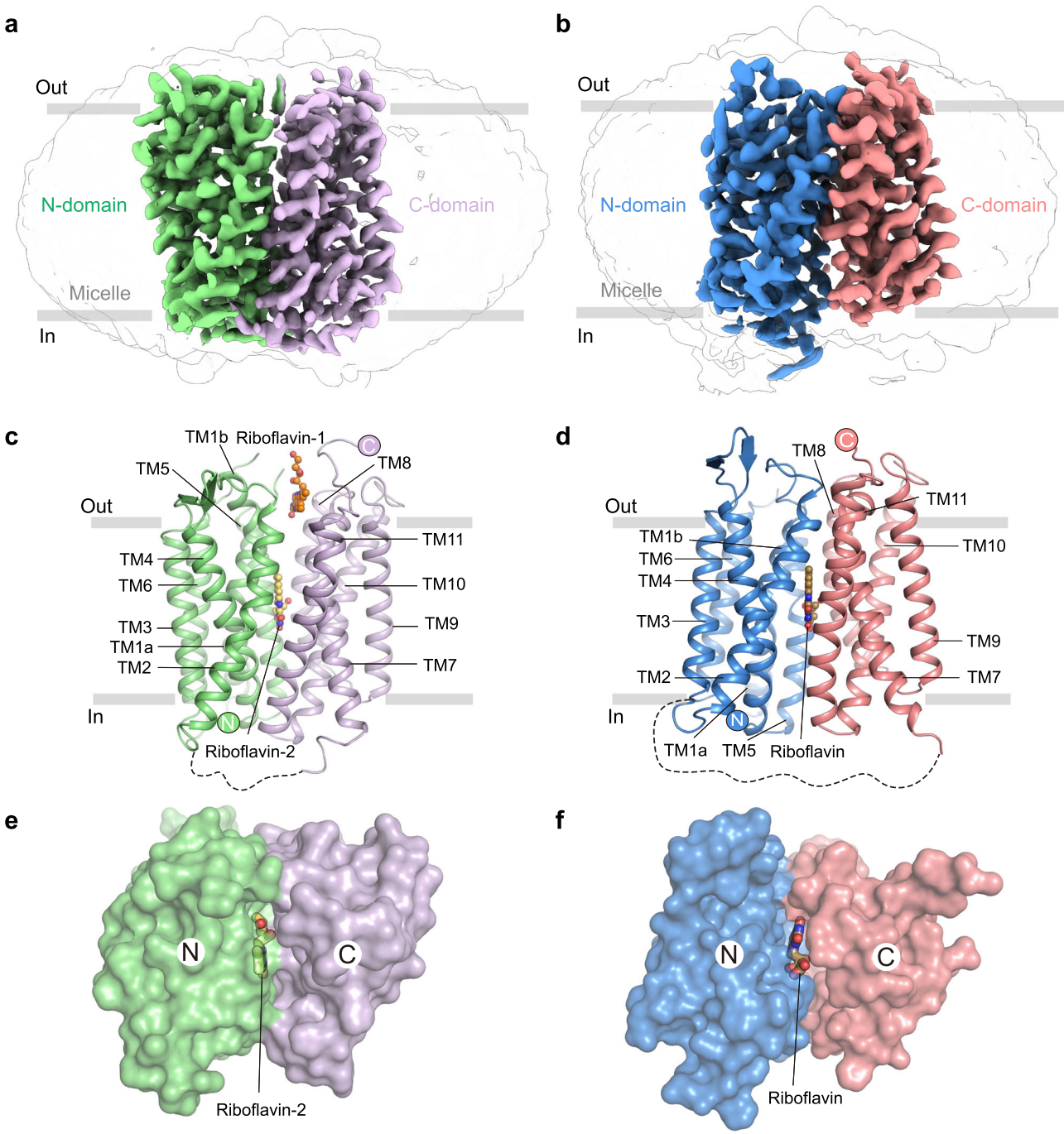

Fig. 2 | EM maps and structures of RFVT2 and RFVT3. a, **b** The EM maps of RFVT2 (**a**) and RFVT3 (**b**). The N- and C-domains of RFVT2 are colored in green and purple. The N- and C-domains of RFVT3 are colored in blue and red. The same color scheme is applied throughout the paper unless specified. **c**, **d** Cartoon representation of RFVT2 (**c**) and RFVT3 (**d**). Riboflavin is depicted in sticks. Black dashed lines indicate unsolved flexible regions. **e**, **f** Surface representation of RFVT2 (**e**) and RFVT3 (**f**). RFVT2 and RFVT3 are viewed from the extracellular side and cytosol, respectively. Riboflavin-1 is omitted in RFVT2 for clarity.

uptake by RFVTs than FAD does[6,25], but both FMN and FAD are poorly transported by RFVTs[26]. We observed extra space near the ribityl moiety in the riboflavin pocket which may not be large enough to accommodate the phosphate group in FMN or the adenine group in FAD (Figs. 1a and 3c, f). Even if possible, the binding of FMN or FAD to RFVTs would most likely prevent conformational transitions, thereby stalling the transport reaction.

Unexpectedly, we observed a possible second riboflavin bound to the outward-occluded RFVT2, residing in the extracellular vestibule between the N- and C-domains (Fig. 3a and Supplementary Fig. 2f). A closer look revealed that this potential riboflavin interacts with W45 from the N-domain and several residues from the C-domain (Supplementary Fig. 5a–c). To validate this possible site, we generated the W45A and F300A/L303A mutants and assayed their activities. W45A slightly reduced [^{13}C]riboflavin accumulation by ~20%, but F300A/L303A has negligible effect on [^{13}C]riboflavin transport (Supplementary Fig. 5d). We further measured the kinetics of RFVT2-W45A, yielding an apparent *K*m of 0.13 μM and *V*max of 6.6 pmol/mg protein/min (Supplementary Fig. 5e), which are decreased to ~20% and ~50% to those of RFVT2^{WT}, respectively, indicating a role of W45 in substrate transport. It is very unlikely that two riboflavin molecules simultaneously bind to RFVTs in a transport cycle, because the extracellular riboflavin would prohibit the

https://doi.org/10.1038/s41467-025-59255-7

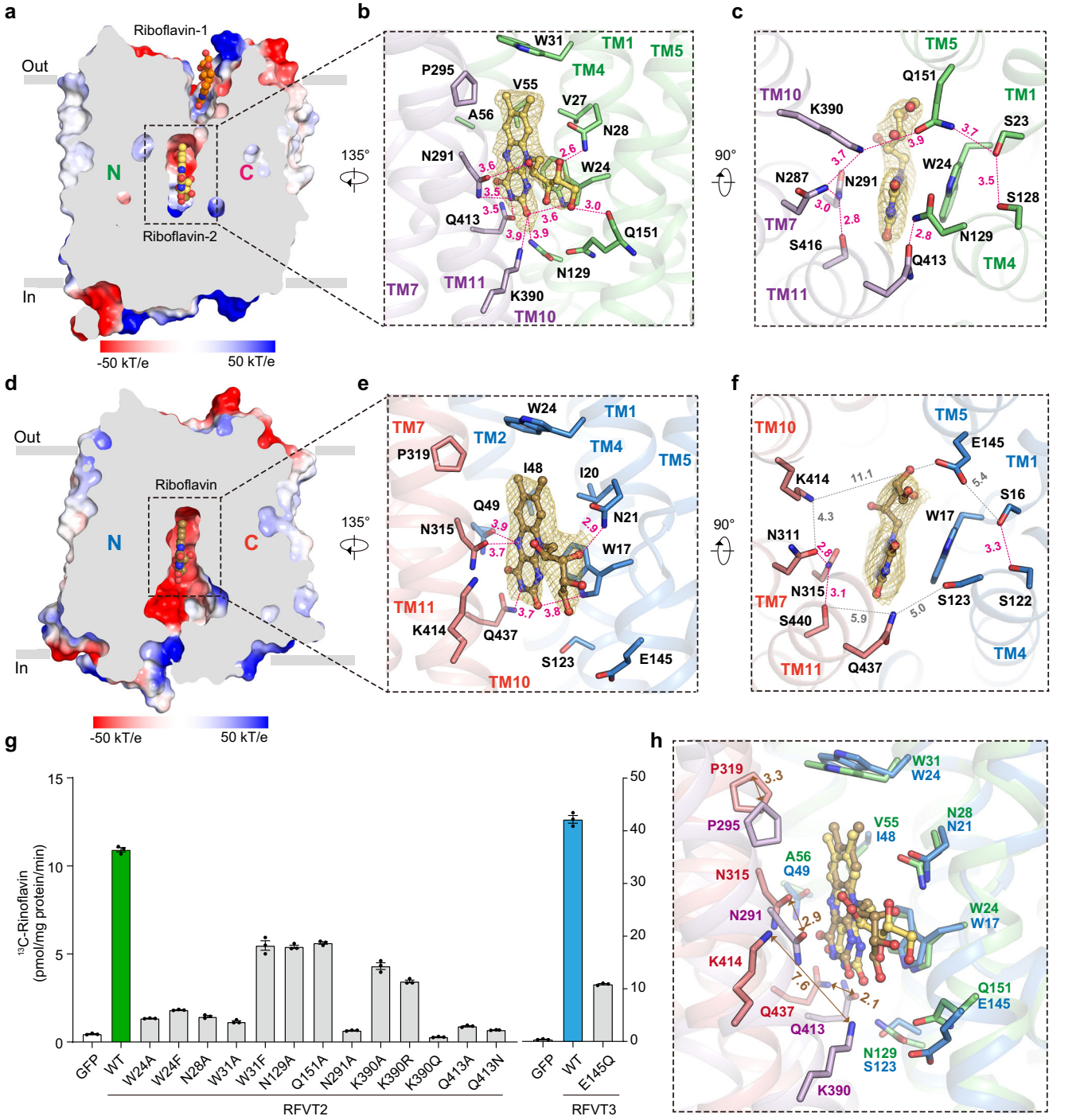

Fig. 3 | Riboflavin recognition by RFVT2 and RFVT3. a, **d** Cut-open electrostatic potential surface of RFVT2 (**a**) and RFVT3 (**d**). Positive and negative potential are colored in blue and red, respectively. Riboflavin is depicted in sticks. **b**, **e** Riboflavin site in RFVT2 (**b**) and RFVT3 (**e**). Residues involved in riboflavin binding are shown side chains in sticks. Red dashed lines indicate polar interactions. **c**, **f** The hydrogen bond network in RFVT2 (**c**) and RFVT3 (**f**). Residues involved in the network are shown side chains in sticks. Gray dashed lines indicate distances. **g** [^{13}C]riboflavin uptake by WT RFVTs and mutants. Cells were subjected to 1 μM [^{13}C]riboflavin for 1 min at pH 7.5. Cells expressing GFP served as controls. Data are presented as mean ± s.e.m.; n = 3 independent replicates. Source data are provided as a Source Data file. **h** The superposition of the riboflavin site of RFVT2 and RFVT3. The N-domain was used as a reference for structural alignment. The brown arrows indicate the distances between residues with conformational shifts.

closure of RFVT2 on the extracellular side when switching to an inward-facing conformation. It has been reported that a potential allosteric pocket opens to the extracellular side in the occluded sugar transporters[29,34] and similar two serotonin sites were revealed in the serotonin transporter SERT[35]. Although we cannot rule out the possibility of a non-specific binding in this site, we speculate that the outer site could be a docking site for riboflavin or a potential allosteric regulation site, which may facilitate the sorting and translocation of riboflavin to the central site.

In the inward-open RFVT3, riboflavin is situated in the central cavity and interacts with neighboring residues that are highly conserved among RFVT1-3 (Fig. 3d–f and Supplementary Fig. 6). The superposition of the two central riboflavin sites in RFVT2 and RFVT3 revealed a nearly identical binding mode for riboflavin (Fig. 3h), in

agreement with the similar substrate specificity of RFVTs[9]. However, several distinct interactions can be found in the riboflavin pockets of the RFVTs. Specifically, N129 of RFVT2 is substituted with S123 in RFVT3, making RFVT3 missing a hydrogen bond interaction with riboflavin; interestingly, Q49 in RFVT3, which replaces A56 of RFVT2, offers an additional hydrogen bond interaction with riboflavin (Fig. 3b, e, h). In addition, the neutral residue Q151 of RFVT2 is substituted with the acidic residue E145 in RFVT3. Although neither of the two residues appear to directly contribute to riboflavin binding, the E145Q mutation significantly decreased the transport activity of RFVT3 to a similar level to that of $RFVT2^{WT}$ (Fig. 3g), indicating that E145 of RFVT3 may have other functional roles beyond substrate binding.

Below the bound riboflavin in the outward-occluded RFVT2, we observed a broad hydrogen bond network that connects the N- and C-domains. This network is composed of S23, S128, N129 and Q151 from the N-domain and N287, N291, K390, Q413 and S416 from the C-domain (Fig. 3c). Interestingly, the hydrogen bond network dissipated in the inward-open RFVT3 (Fig. 3f). For example, the hydrogen bond pairs of N129-Q413 and Q151-K390 in RFVT2 are separated at distances of 5.0 Å and 11.1 Å between the respective residues in RFVT3, respectively. We therefore speculate that this network has a role in stabilizing the outward-facing conformation, the bound riboflavin interacts with most of residues in the network and may disturb the stability of the network, thus triggering state transitions.

MD simulations of riboflavin binding

To reveal detailed differences in the binding of riboflavin to distinct states, we aligned the two structures using the N-domain as a reference, which clearly demonstrated that some of the riboflavin-interacting residues underwent marked conformational shifts during state transitions. For instance, N315 and K414 of RFVT3 shifted by 2.9 Å and 7.6 Å, respectively, relative to N291 and K390 of RFVT2 (Fig. 3h). This raises one question: Does riboflavin have a higher binding free energy in inward RFVTs owing to a looser binding pocket than that of outward RFVTs? To answer this question, we performed a molecular dynamics (MD) simulation-based binding free energy analysis of riboflavin binding in RFVTs. By applying the Molecular Mechanics-Generalized Born Surface Area (MM/GBSA) method[36] on MD simulation trajectories, we calculated the binding free energies of riboflavin bound to RFVT2 and RFVT3, respectively. The resulting riboflavin binding free energy in the outward-occluded RFVT2 is notably lower than that in the inward-open RFVT3 (Supplementary Fig. 7a, b). We further investigated the contribution of each residue to riboflavin binding and found that W24, N291 and Q413 are the three dominant contributors to riboflavin binding in the outward-occluded RFVT2 (Supplementary Fig. 7c, d), in line with the structural observation and mutagenesis results (Fig. 3b, g). The contributions of the three corresponding residues in the inward-open RFVT3, W17, N315 and Q437, are considerably lower than those in RFVT2 (Supplementary Fig. 7c–f). Furthermore, the root mean square fluctuation (RMSF) analysis of the ligand indicates that the riboflavin in the outward-occluded RFVT2 exhibits lower mobility compared to the ligand in the inward-open RFVT3 (Supplementary Fig. 7g). These results suggest that RFVTs expose their high-affinity sites for riboflavin loading on the extracellular side and promote substrate release on the intracellular side through a relatively lower-affinity site.

To gain insights into riboflavin binding induced conformational changes in RFVTs, we conducted MD simulations on four systems, including RFVT2 with or without riboflavin bound and RFVT3 with or without riboflavin bound. In the four systems, the outward RFVT2 and the inward RFVT3 exhibit no obvious global conformational changes, reflected by their relative stable backbone r.m.s.d. values (Supplementary Fig. 8a–d). The intracellular side of RFVT2 remains closed regardless of riboflavin bound or not, as indicated by a predominant distribution during clustering for each of the two MD systems (Supplementary Fig. 8e). However, we observed local dynamics in the gating helices TM1 and TM7 on the extracellular side. In particular, the lid residue W31 from TM1 strongly favors a hydrogen bond interaction with Q298 from TM7 in the presence of riboflavin, while this hydrogen bond appears intermittently without riboflavin (Supplementary Fig. 8f). Notably, the equivalent W24 and Q322 in the inward-open RFVT3 structure indeed engage in a hydrogen bound, suggesting that this conserved Trp has a role in RFVT state transitions. In contrast to RFVT2, RFVT3 displays a major group with an open intracellular gate in the presence of riboflavin which is similar to the structure of RFVT3 with riboflavin bound, and a minor group with a narrower intracellular gate which is close to that of RFVT2 structure; without riboflavin, however, RFVT3 shifts the major group notably closer to the closed intracellular gate of the outward RFVT2 structure (Supplementary Fig. 8e). These observations suggested that the binding of riboflavin to outward-facing RFVTs may induce local conformational changes in the gating helices which facilitate state transitioning to an occluded state, and the release of riboflavin from the inward-open RFVTs tends to stimulate state switching to inward-occluded or occluded states.

Low pH enhanced activity of RFVT3

Previous studies[6,7,25] and our own results demonstrated that RFVT3, rather than RFVT1 or RFVT2, exhibits pH-dependent activity (Fig. 4a–c). We have also elucidated that RFVT3 is about 3-fold more efficient at pH 5.5 than at pH 7.5, whereas the activity of RFVT2 is not affected by pH (Fig. 1c–e). The structures of the RFVTs allowed us to investigate how proton enhances the activity of RFVT3. After careful inspection, we found that D119 on TM4 and E145 on TM5 are protonatable residues inside the central cavity of RFVT3, which are substituted with C125 and Q151 in RFVT1 and RFVT2, respectively (Supplementary Fig. 6). In the inward-open state, E145 points to the aqueous cleft, whereas D119 is situated in a small extended cavity enclosed by TM1, TM3, TM4 and TM6 (Supplementary Fig. 9a, c). To reveal the positions of these two acidic residues in the outward-facing state, we aligned the N- and C-domains of RFVT3 to those of RFVT2 separately, generating an outward-facing model of RFVT3 (Fig. 4d). In the outward-facing model, E145 is situated in the interior and is solvent accessible, whereas D119 remains unchanged in the N-domain (Fig. 4d and Supplementary Fig. 9e). Notably, the Cα atoms of E145 and K414 of RFVT3 coincide with those of Q151 and K390 of RFVT2 (Fig. 4e). In the outward RFVT2, Q151 forms a hydrogen bond with K390, suggesting that E145 potentially engages in electrostatic interactions with K414 in the outward RFVT3 (Fig. 4e). Conversely, E145 and K414 are separated from each other at a distance of 11.1 Å in the inward-open state (Fig. 4f). These observations indicate that the hydrogen bond between Q151 and K390 or the salt bridge between E145 and K414 may have a role in stabilizing the outward-facing conformation of RFVTs. As for D119, it forms multiple interactions with W17, T19 and the backbone carbonyl oxygen atom of S16 from the hinge region in the gating helix TM1, and such interactions are not present in RFVT2 (Fig. 4f and Supplementary Fig. 9a–e).

To investigate the role of D119 and E145 in the proton-dependent activity of RFVT3, we assayed the transport activities of the D119C and E145Q mutants under different pH conditions. The uptake results clearly demonstrated that D119C and E145Q completely abolished the pH-dependency of RFVT3 (Fig. 4a). Furthermore, concentration-dependent riboflavin uptake assay revealed dramatic kinetics changes for the D119C and E145Q mutants. RFVT3-E145Q exhibits *K*m values of 0.3 μM at pH 5.5 and of 1.35 μM at pH 7.5, which are similar to those in WT RFVT3; however, it has similar *V*max values of ~22 pmol/mg protein/min at the two pH conditions, which are only one fourth of that of WT RFVT3 (Fig. 4b). On the other hand, RFVT3-D119C displays essentially identical *K*m and *V*max values at pH 5.5 and 7.5, both of which are significantly lower than those of WT RFVT3 (Fig. 4c). These

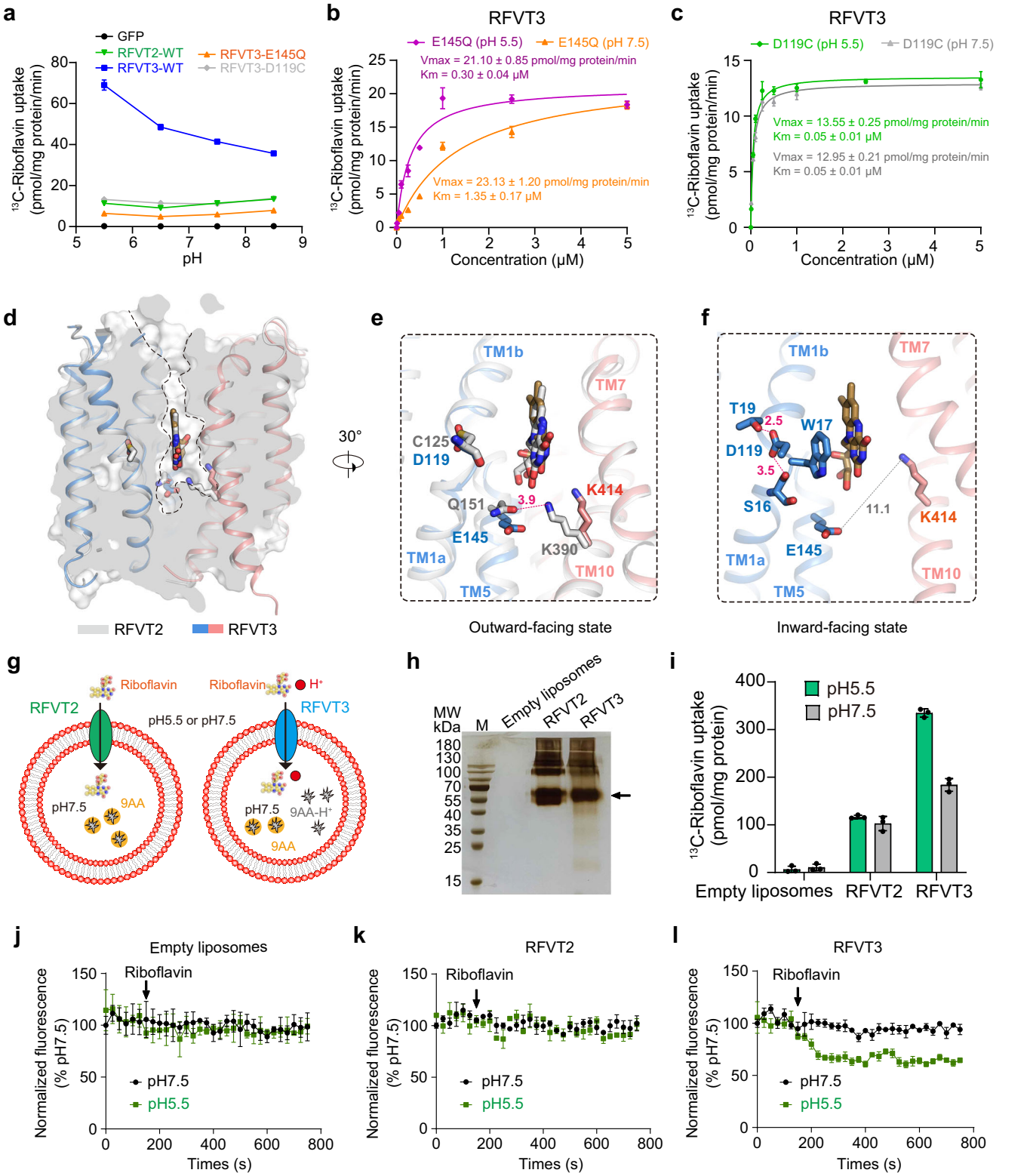

kinetics results indicate that E145 and D119 have different roles in the proton-dependent activity of RFVT3.

To further examine whether proton is co-transported in RFVT3, we conducted proteoliposome transport assay. We first reconstituted purified human WT-RFVT2 and RFVT3 proteins into liposomes, respectively (Fig. 4g). Silver staining gels indicate that RFVTs were successfully reconstituted in liposomes (Fig. 4h). Next, we investigated [^{13}C]riboflavin uptake using the proteoliposomes under different pH conditions, demonstrating that both RFVT proteoliposomes have robust activity. In particular, RFVT3 proteoliposomes exhibit higher uptake activity at pH 5.5 than at pH 7.5, whereas the activity of RFVT2 proteoliposomes is insensitive to pH (Fig. 4i). These results are in accord with the HEK293T whole-cell uptake assay (Fig. 1b). Furthermore, we probed proton influx during riboflavin uptake in the proteoliposomes using a pH indicator 9-aminoacridine (9AA)[37], which was included inside the proteoliposomes (Fig. 4g). Upon adding riboflavin,

Fig. 4 | Structural basis for pH-dependent activity of RFVT3. a The pH-dependent riboflavin transport activity of RFVTs. Cells were incubated in indicated pH conditions containing 1 μM [^{13}C]riboflavin for 1 min. Cells expressing GFP served as controls. Data are presented as mean values ± s.e.m.; $n = 3$ independent replicates. **b**, **c** Concentration-dependent uptake of [^{13}C]riboflavin by HEK293T cells expressing RFVT3-E145Q (**b**) and RFVT3-D119C (**c**) under pH 5.5 and pH 7.5. Data are presented as mean ± s.e.m.; $n = 3$ independent replicates. **d** Cut-open sliced surface of RFVT2. The N-domain (Blue) and C-domain (Red) of RFVT3 were superimposed to those of RFVT2 (Gray). Riboflavin is depicted in spheres. The black dashed lines indicate the cavity of RFVT2. **e** Hydrogen bond interaction between Q151 and K390 in the outward-occluded RFVT2. RFVT3 is aligned with RFVT2 to show potential interaction between E145 and K414 in the outward conformation. **f** The interaction of D119 with TM1 and the decoupling of E145 and K414 in the inward-open RFVT3. Riboflavin and side chains of related residues are shown in sticks. Red dashed lines indicate possible hydrogen bond interactions. Gray dashed lines indicate the distance between E145 and K414. **g** A schematic diagram of proteoliposome transport assay. Riboflavin is depicted in sticks. 9AA probes in circled stars. Red balls represent protons. RFVT2 and RFVT3 in green and blue, respectively. **h** Silver-stained SDS gel of RFVT proteoliposomes. Black arrow indicates molecular weight (MW) of RFVTs. **i** [^{13}C]riboflavin uptake in RFVT proteoliposomes. Proteoliposomes were subjected to 1 μM [^{13}C]riboflavin for 10 min at pH 7.5 or pH 5.5. Empty liposomes served as controls. Data are presented as mean ± s.e.m.; $n = 3$ independent replicates. **j**–**l** Proton influx assay in empty liposomes (**j**), RFVT2 proteoliposomes (**k**) and RFVT3 proteoliposomes (**l**). Black arrow indicates adding of riboflavin. Data are normalized to fluorescence values at pH 7.5 and are presented as mean ± s.e.m.; $n = 3$ independent replicates. Source data are provided as a Source Data file.

the fluorescence of 9AA inside the empty liposomes and RFVT2 proteoliposomes remained stable at either pH 5.5 or pH 7.5, suggesting no proton influx event (Fig. 4j, k); by contrast, the fluorescence in RFVT3 proteoliposomes quenched substantially at pH 5.5 in comparison to that of at pH 7.5, strongly indicating proton influx accompanying riboflavin uptake (Fig. 4l). These results suggest that protons are co-transported in RFVT3 at low pH, but not in RFVT2.

Protons energize substrate translocation in many transporters by means of distinct mechanisms[38,39]. For example, protons are reported to be directly involved in substrate binding in oligopeptide transporters[40] and substrate release in vesicular monoamine transporter VMAT2[27]; in other cases, protonation alters local electrostatic networks that allosterically affects substrate coordination[38] or triggers local conformational changes in gating helices[29]. Based on these structural and functional results, we propose a possible explanation for the pH-enhanced activity in RFVT3. When RFVT3 assuming an outward-open conformation, E145 and K414 form a potential salt bridge that contributes to stabilizing the outward-open conformation. Meanwhile, protons could access to the central cavity and possibly protonate D119 and E145. Because of the close interactions between D119 and the hinge region in the gating helix TM1 (Fig. 4f), protonation of D119 potentially disturb such interactions and trigger local conformational changes that may allosterically promote riboflavin binding and state transitions, supported by the pH-independent kinetics (*K*m and *V*max) of D119C (Fig. 4c). On the other hand, protonation of E145 may affect the salt bridge interaction with K414, which may further accelerate the conformational transition to an occluded state. Despite sharing low sequence identity and no recognizable consensus sequences with MFS transporters, similar protonation induced salt bridge breakage was found in the proton-dependent human folate transporter PCFT[41] and the plant nitrate transporter NRT1.1[42]. RFVT1 and RFVT2 are insensitive to pH most likely due to the substitutions of D119 and E145 with C125 and Q151 (Supplementary Figs. 6 and 9e).

Transport mechanism of RFVTs

To understand how RFVTs transport riboflavin, we aligned the structures of RFVT2 and RFVT3 using the N-domain as a reference. The superposition revealed that while the N-domains are well overlaid, the C-domain displays an oscillation of ~15° (Fig. 5a), indicating a rigid body-like interdomain movement during state transitions in the transport cycle. On the extracellular side, RFVT2 holds an open gate of 8 Å at the narrowest region between the N- and C-domains, which allows the flat riboflavin to pass through (Fig. 5b). In contrast, the extracellular gate of RFVT3 is closed by TM1-2 and TM7-8, which form a ring of hydrophobic interactions involving P28, V31 and P41 from the N-domain and L327, Y334 and A338 from the C-domain. Additionally, two hydrogen bond interactions between T323 and the main chain carboxyl oxygen atom of W38 and between Y39 and R455 further stabilize the closed extracellular gate of RFVT3 (Fig. 5b). On the other side, the intracellular gate of RFVT2 is sealed by TM4-5 and TM10-11, including hydrophobic interactions between L133, L144 and F148 from the N-domain and V391, S394 and L405 from the C-domain. Furthermore, the hydrogen bond between H398 and the main chain carboxyl oxygen atom of L136 and the salt bridge between E77 and R402 enhance the closure of RFVT2 on the intracellular side (Fig. 5c). On the intracellular side of RFVT3, however, the decoupling of these interactions results in an elongated open gate, allowing the release of the bound riboflavin to the cytosol (Fig. 5c). Of note, the charged residues involved in the salt bridge interactions are strictly conserved in the SLC52 family (Supplementary Fig. 6). To validate the role of these charged residues, we examined the transport activities of the E77A, R402A and E77R/R402E mutants of RFVT2. The results demonstrated that E77A and R402A reduced ~50% [^{13}C]riboflavin uptake in comparison to RFVT2^{WT}, while the charge-exchange double mutation E77R/R402E restored ~80% transport activity of RFVT2^{WT} (Fig. 5d).

According to the well-documented alternating-access transport mechanism, the pseudo-symmetric N- and C-domains of the MFS transporters alternatively open either side in a “rocker-switch”-like manner[29]. On the basis of the structural observations, we speculate that RFVTs employ a similar alternating-access mechanism for transporting riboflavin (Fig. 6). When assuming an outward-facing conformation, RFVTs are stabilized by the interdomain hydrogen bond network and the specific salt-bridge of E145-K414 for RFVT3, as well as the salt-bridge interactions near the intracellular side. In this state, the high-affinity site is exposed to the extracellular space for riboflavin binding to (Fig. 6, left). Once riboflavin bound to the central site, it interacts with the Trp-Asn pair and other residues in the hydrogen bond network. The substrate binding induces local conformational changes in the gating helices TM1 and TM7, which lowers the energy barrier for global conformational changes to substrate-bound outward-occluded and fully occluded states (Fig. 6, upper-middle). Although the proton coupling mechanism of RFVT3 remains elusive, protonation of D119 and E145 could accelerate state transitions by potentially facilitating substrate binding and affecting the salt-bridge of E145-K414. To date, the fully occluded structures of MFS transporters are much less than the outward and inward structures[29,43], suggesting that the occluded state is possibly metastable. Similarly, the transient occluded RFVTs subsequently switch to an inward-facing state with the salt-bridge breakage and gating helices rearrangements on the intracellular side and local conformation changes in the substrate binding site (Fig. 3h), which may decrease the binding affinity of riboflavin and facilitate the release of riboflavin to the cytosol (Fig. 6, right). The release of riboflavin allows RFVTs switch to unloaded occluded states involving global conformational changes between the two domains and reestablishment of the salt-bridge on the intracellular side (Fig. 6, lower-middle), which again are metastable and swing back to the outward-facing state, thus finishing a transport cycle.

https://doi.org/10.1038/s41467-025-59255-7

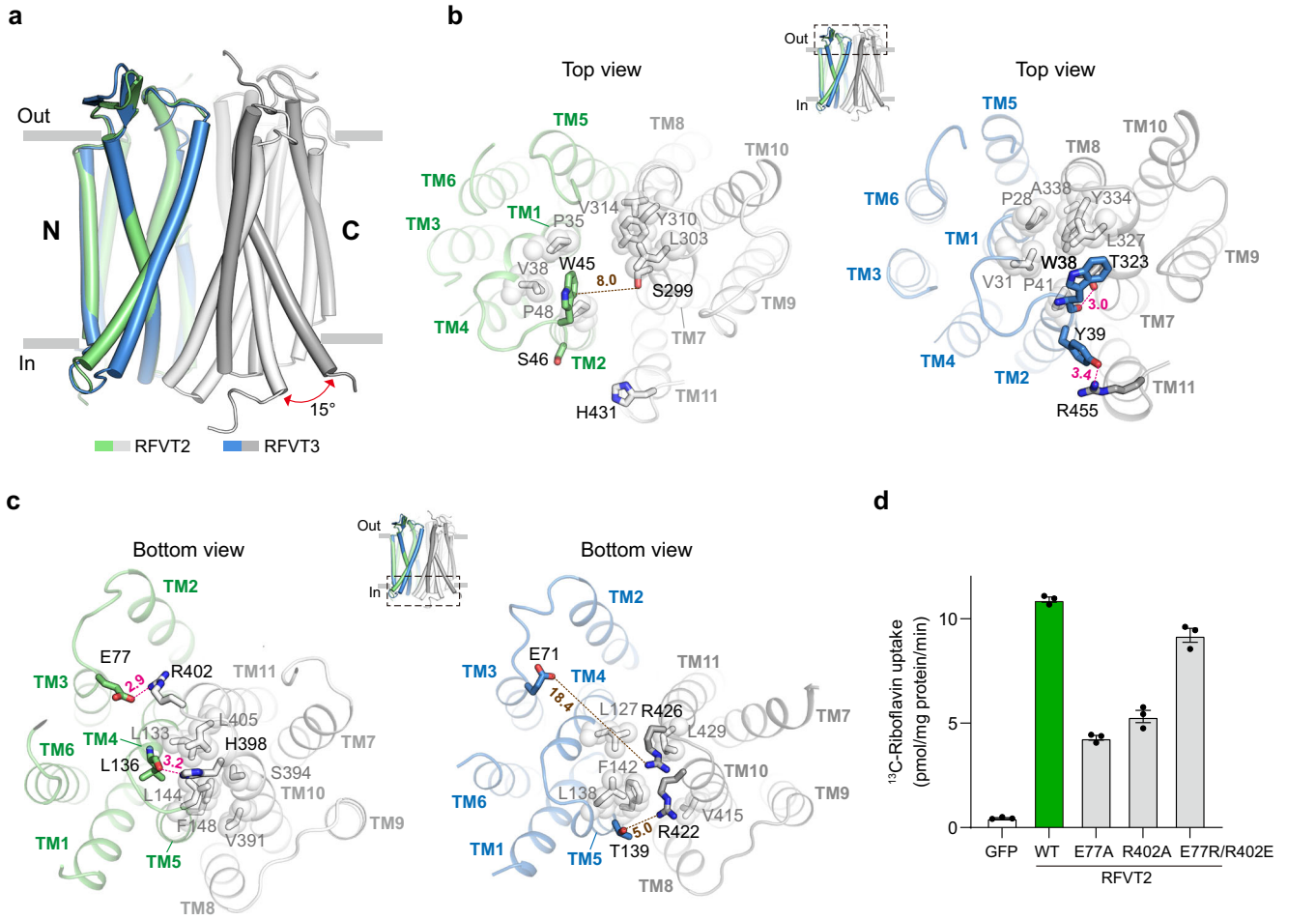

Fig. 5 | Extracellular and intracellular gates of RFVTs. a The superposition of RFVT2 and RFVT3 using the N-domain as a reference. Red arrow indicates the oscillation between the C-domains. The N-domain of RFVT2 and RFVT3 are colored in green and blue, respectively. The C-domain of RFVT2 and RFVT3 are colored in light gray and gray, respectively. **b**, **c** The interaction network in the extracellular gate (**b**) and the intracellular gate (**c**) of RFVT2 (left) and RFVT3 (right). Red dashed lines indicate hydrogen bond or electrostatic interactions. Brown dashed lines indicate distances. Residues involved in gate interactions are shown side chains in sticks. **d** [^{13}C]riboflavin uptake by RFVT mutants in the intracellular interaction network. Cells were subjected to 1 μM [13C]riboflavin for 1 min at pH 7.5. Cells expressing GFP served as controls. Data are presented as mean ± s.e.m.; n = 3 independent replicates. Source data are provided as a Source Data file.

Discussion

In this study, we described the structures of human RFVT2 and RFVT3, which were captured in two distinct functional states. Complemented with the functional and MD simulation assays, our work provides mechanistic insights into riboflavin recognition and transport by RFVTs. The structure, riboflavin binding mode and the transport mechanism of the human RFVTs are completely different from those of the bacterial riboflavin transporter RibU[24,44]. Instead, human RFVTs show remarkable structural similarity to ENT1 of the SLC29 family, which adopt an atypical MFS-like fold and employ the "rocker-switch" alternating-access transport mechanism (Fig. 6). These findings have important physiological and pathologic implications. First, the riboflavin binding pocket is highly conserved among RFVT1-3, in line with their similar riboflavin specificity[6,25], which also explains why FMN and FAD could be poorly transported by RFVTs[6,26]. Second, our site-direct mutagenesis and proteoliposome transport assays clearly demonstrated that the protonatable D119 and E145 dictate the proton-dependent activity of RFVT3, whereas RFVT1 and RFVT2 are pH-insensitive presumably because the corresponding residues are substituted with C125 and Q151. However, the exact roles of the two acidic residues and the stoichiometry of proton and riboflavin in RFVT3 remain elusive and require future investigations. Considering that RFVT3 is highly expressed in the small intestine, testis, kidney and placenta[6], RFVT3 could utilize the proton gradient as a driving force to efficiently take up riboflavin in these tissues. The activity of the other two RFVTs is Na^+, Cl^- and proton independent[5–7], suggesting that they are solely carrier-mediated riboflavin transporters. Riboflavin is not largely stored in human tissues, the absorption, distribution and metabolism of riboflavin by the three RFVTs has fundamental role in riboflavin, FMN and FAD homeostasis. Finally, many mutations in RFVTs that may alter their expression, localization or function have been associated with human diseases, including multiple acyl-CoA dehydrogenase deficiency (MADD) and Brown-Vialetto-van Laere syndrome[9]. We have mapped 28 pathogenic mutations of RFVT2 and 49 pathogenic mutations of RFVT3 to their respective structures (Fig. 7), demonstrating the broad distribution of the mutations in the structures, which suggest that RFVTs are a delicate machinery for riboflavin transport. Of note, the N28S, W31S and S52F mutations of RFVT2 and the W17R, I20L, N21S, W24X (X, nonsense mutation) and P319S mutations of RFVT3 may alter RFVT function by affecting riboflavin recognition. The E77K mutation of RFVT2 would abolish the salt bridge of E77-R402, thereby disturbing the conformational equilibrium. We also observed many Pro or Gly mutations in the TM helices, which likely change the rigidity or flexibility of the transmembrane helices that are necessary for normal transport activity (Fig. 7).

https://doi.org/10.1038/s41467-025-59255-7

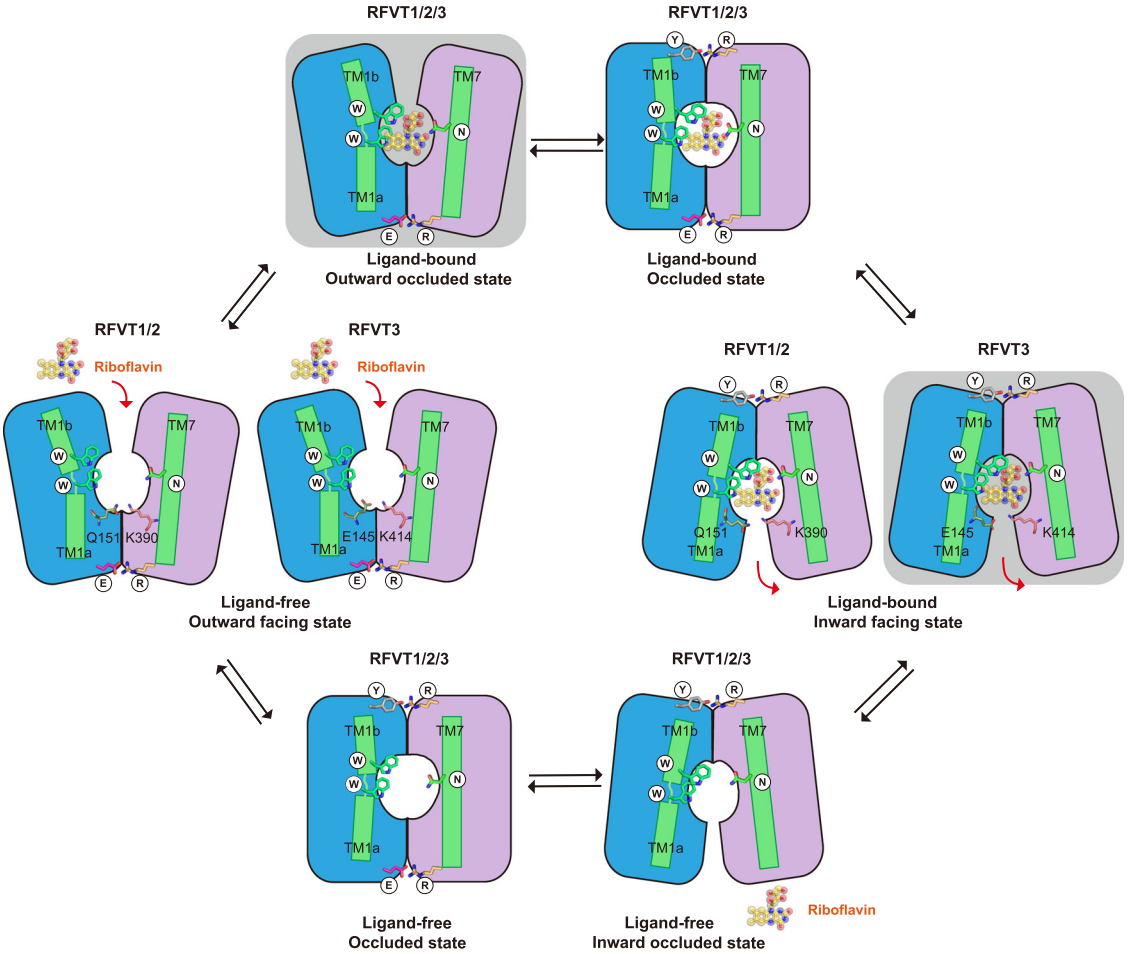

Fig. 6 | Proposed model for riboflavin transport in RFVTs. The outward-facing RFVTs are stabilized by interdomain hydrogen-bound network and salt-bridge interactions. In this state, extracellular riboflavin accesses and binds to the high-affinity site in the central cavity. The binding of riboflavin in RFVTs induces conformational transition to an outward-occluded state (RFVT2 structure) and then to an occluded state. After switching to the inward-facing state (RFVT3 structure), riboflavin dissociates from RFVTs and enters the cytosol. The release of riboflavin triggers RFVTs transitioning to an intermediate ligand-free occluded state and then back to the outward-facing state. The N- and C-domain in blue and purple. The gating helices TM1 and TM7 are colored in green. The conserved Trp and Asn interacting with riboflavin and the lid Trp are indicated in black cycles. Riboflavin in spheres. The hydrogen bond or electrostatic interaction forming residues are shown in sticks.

Utilizing the GFP-nanobody as the fiducial marker, we have successfully determined the structures of the human riboflavin transporters in this study and the human VMAT2 in a previous study[27]. Alongside the antibody strategy[41], other fusion protein strategies have also permitted cryo-EM analysis of small membrane proteins at high-resolution[45–51], indicating that the door to visualizing the structures of even smaller proteins has been opened. This would advance our understanding of broader biological processes and aid in the development of potential therapies for difficult targets regarding structure accessibility. Taken together, the structure and the transport mechanism has provided valuable insights into human RFVT function, pathology and riboflavin homeostasis.

Methods

Cloning, expression and purification of human RFVTs

The genes of human *SLC52A2* (UniProt accession code: Q9HAB3) and *SLC52A3* (UniProt accession code: Q9NQ40) were subcloned and inserted into a modified pEG2 BacMam vector. For transport assay, the N-termini of full-length wild-type RFVT2 and RFVT3 were fused with a twin-strep purification tag and a green fluorescent protein (GFP). For cryo-EM analysis, the twin-strep tag and GFP were fused to the N-terminus, and a nanobody specific to GFP was fused to the loop between E228 and P262 of RFVT2 and between P267 and A293 of RFVT3, namely RFVT2^{EM} and RFVT3^{EM}, respectively (Supplementary Fig. 1a, b). Site-directed mutations were generated by a standard mutagenesis kit (Vazyme Biotech Co., Ltd). All the wild-type and mutation plasmids were confirmed by DNA sequencing. The primer sequences are listed in Supplementary Table 2. The plasmids were transformed into DH10Bac competent cells to generate bacmids. The *Spodoptera frugiperda Sf*9 insect cells (Invitrogen, USA) were transfected with the plasmids and to produce P1-P3 viruses. To express the transporters, HEK293F cells (Gibco, USA) were cultured in OPM-293 medium (OPM) supplemented with 5% CO_2 at 37 °C and were transduced with the P3 viruses at a ratio of 1:200 (v/v) when the cell density was 2.5×10^6 mL^{-1} (C100, RWD). After 8–12 h, 10 mM sodium butyrate (Sigma, USA) was added to the medium to increase protein expression. The cells were cultured for another 48 h before harvest.

For purification of human RFVTs, cells were homogenized using a Dounce homogenizer, and the cell membrane was collected by ultracentrifugation at 100,000×*g* for 45 min. Then, the membrane was resuspended and solubilized in buffer A (20 mM HEPES pH 7.5, 150 mM NaCl, 5 mM β-mercaptoethanol (β-ME), and a protease inhibitor cocktail including 2 μM aprotinin, 2 μM leupeptin, 0.8 μM pepstatin and 1 mM phenylmethylsulfonic acid acyl fluoride (PMSF)) supplemented with 1% (w/v) n-dodecyl-β-D-maltoside (DDM, Anatrace), 0.15% (w/v) cholesterol hemisuccinate (CHS, Anatrace) and 10 μM riboflavin

https://doi.org/10.1038/s41467-025-59255-7

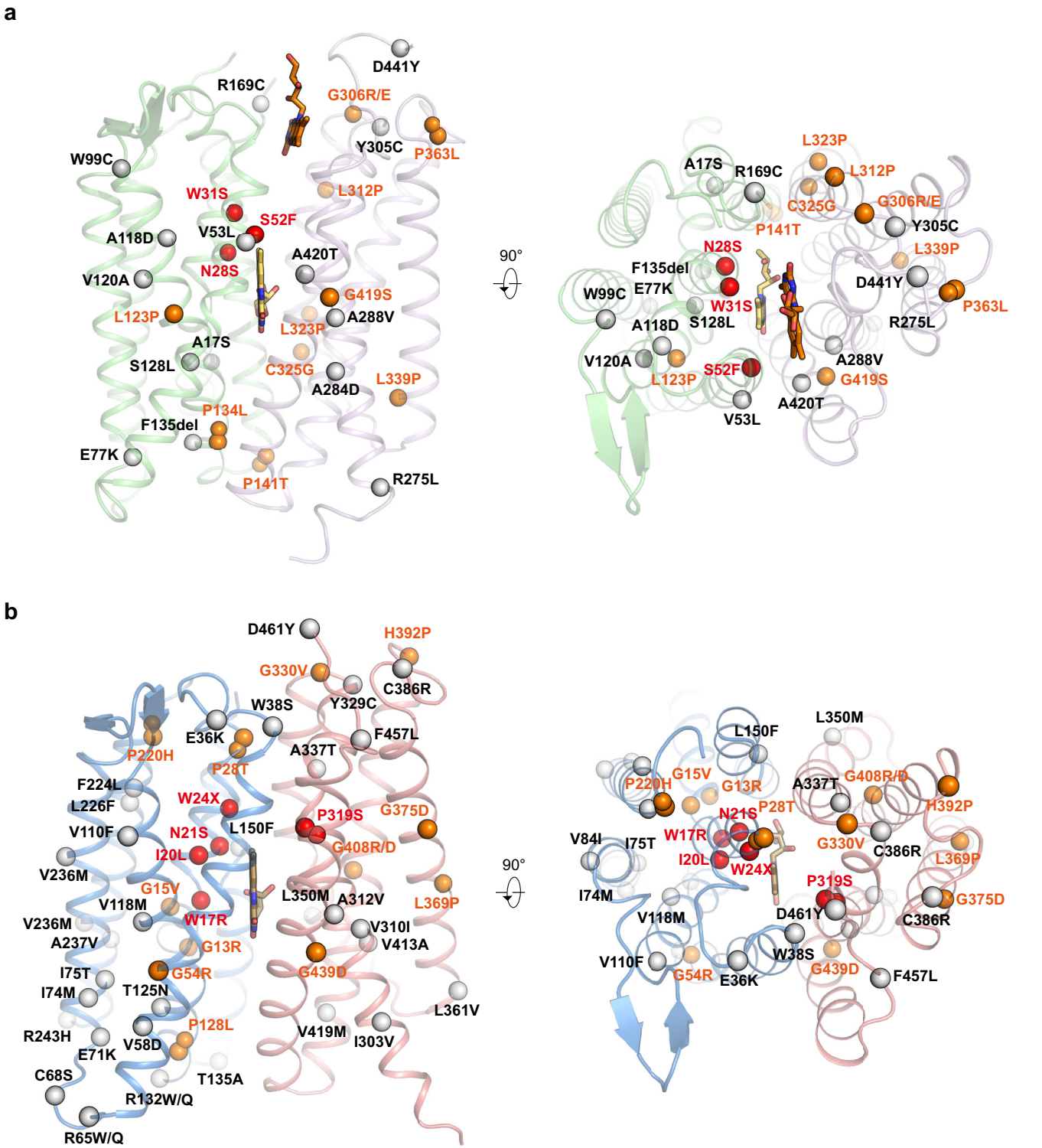

Fig. 7 | Mapping pathogenic mutations on the RFVT2 and RFVT3 structures. a In total, 28 pathogenic mutations of RFVT2 were mapped on the structure. **b** In all, 49 pathogenic mutations of RFVT3 were mapped on the structure. Red balls represent residues contributing to riboflavin binding, orange balls represent Pro/Gly related mutations, gray balls represent other mutations. Riboflavin is depicted in sticks.

(MCE). The mixture was gently stirred for 2 h at 4 °C. After another ultracentrifugation at 100,000×*g* for 30 min, the supernatant was incubated with Strep-Tactin beads (Smart-Lifesciences, China) pre-equilibrated with buffer B (buffer A supplemented with 5 mM $MgCl_2$, 1 mM ATP, 5 μM riboflavin and 0.01% (w/v) lauryl maltose neopentyl glycol (LMNG, Anatrace)). Subsequently, the beads were washed with 8 column volume (CV) buffer B and another 5 CVs of Buffer C (buffer A supplemented with 5 μM riboflavin and 0.01% (w/v) LMNG). The protein samples were eluted with 4 mL of buffer D (buffer C supplemented with 5 mM D-desthiobiotin). The eluted samples were concentrated and loaded onto a Superose 6 Increase 10/300 GL column (Cytiva) preequilibrated with 20 mM HEPES pH 7.5, 150 mM NaCl, 0.002%

LMNG (w/v), and 2 mM β-ME. Peak fractions were collected and concentrated to ~10 mg/mL for cryo-EM grid preparation.

Plasma-membrane localization in HEK293T

HEK293T (Gibco, USA) cells were cultivated on poly-D-lysine-coated 24-well plates and were transfected with plasmids of WT-RFVT2 or its mutant fused with an N-terminal GFP when cell confluence reached ~50%. After 24 h, transfected cells were washed three times with PBS buffer and then were fixed in 4% polyformaldehyde (PFA) for 30 min. Following washed three times with PBS buffer, cells were sealed with antifade mounting medium and observed with a Zeiss LSM980 confocal laser microscope (Zeiss, Germany).

Transport assays in HEK293T

Riboflavin uptake assay was performed in HEK293T cells overexpressing human RFVT2, RFVT3 or their mutants as described in our previous study[52] with modifications. Briefly, HEK293T cells were cultivated on poly-D-lysine-coated 24-well plates and were transfected with P2 or P3 viruses when the cell confluence reached 80–90%. After 48 h, the cells were washed once with Krebs-Ringer buffer (120 mmol/L NaCl, 4.5 mmol/L KCl, 0.5 mmol/L $MgCl_2$, 0.7 mmol/L Na_2HPO_4, 1.5 mmol/L NaH_2PO_4, and 10 mmol/L D-glucose (pH 7.3 ± 0.2)) and then incubated in the Krebs-Ringer buffer containing 0 μM, 0.01 μM, 0.05 μM, 0.1 μM, 0.25 μM, 0.5 μM, 1 μM, 2.5 μM and 5 μM riboflavin-(dioxopyrimidine-$^{13}C_4$, $^{15}N_2$) (Sigma-aldrich, USA) for 1 min at 37 °C. For the uptake assay by RFVT2, RFVT3 or their mutants, cells were incubated in the Krebs-Ringer buffer containing 1 μM riboflavin-(dioxopyrimidine-$^{13}C_4$, $^{15}N_2$) for 1 min. For the pH dependence of riboflavin uptake assay, cells were incubated in the Krebs-Ringer buffer at a range of different pH values (pH 5.5, pH 6.5, pH 7.5 or pH 8.5; the pH value was adjusted with HCl or NaOH) containing 1 μM riboflavin-(dioxopyrimidine-$^{13}C_4$, $^{15}N_2$) for 1 min. Then the cells were washed three times with ice-cold phosphate-buffered saline (PBS) buffer, extracted riboflavin with 1 mL of pre-chilled (−80 °C) 80% (*v*/*v*) methanol solvent containing 1% formic acid, and the extractions were placed at −80 °C for 30 min. Cells were then scraped down from the plate and transferred to a brown tube. After a centrifugation at 16,000×*g* (M1324R, RWD) for 20 min at 4 °C, the supernatant was transferred to a new brown tube for vacuum concentration and then stored at −80 °C until quantitative mass spectrometry analysis. The precipitate was lysed with 0.1 M KOH and protein concentration was calibrated using the BCA protein assay (Thermo Scientific, USA). HEK293T cells expressing only GFP served as controls. The expression levels and oligomeric state of WT RFVTs and all the mutants in this study were assayed by in-gel fluorescence imaging and fluorescence-detection size-exclusion chromatography (fSEC), the related results are presented in Supplementary Fig. 1e–l. The statistics for riboflavin uptake kinetics of WT RFVTs and mutants are analyzed in Prism 8.0.1 (GraphPad Software).

Proteoliposome transport assay

To prepare liposomes, egg lecithin (Medchemexpress, USA) was dissolved in chloroform and subjected to overnight rotary evaporation. The lipid film was dissolved in the reconstitution buffer (20 mM HEPES, 100 mM NaCl, pH 7.5) and diluted to 20 mg/mL. For proton influx assay, a pH sensitive fluorescent dye 9-Aminoacridine (9AA, Medchemexpress) was added at a final concentration of 4 μM. After repeated ten cycles of freeze–thaw (liquid nitrogen and 37 °C), the lipid solution was treated with Avanti Mini-Extruder (31 times) through a 400 nm polycarbonate membrane, and dissolved into Triton-100 with a volume ratio at 1:100 (v:v). RFVT2-WT and RFVT3-WT samples were prepared similarly (Supplementary Fig. 1n, o). The standard composition for reconstitution was: 3 mg egg lecithin, 0.2 mg RFVT2-WT or RFVT3-WT, 0.002% (w/v) LMNG and the reconstitution buffer in a final volume of 1 mL. The control group with liposomes only was replaced with recombinant buffer instead of proteins, while other components remained unchanged. The mixture of lipids and proteins was incubated at 4 °C for 2 h for recombination. The recombinant solutions were subjected to three batches of Bio-Beads SM2 (2 × 500 mg and 1× 600 mg; Bio-Rad) to remove detergents. After overnight incubation with the third Bio-Beads, the proteoliposomes were collected by ultracentrifugation at 264,000×*g* (Beckman) for 30 min and were resuspended in the reconstitution buffer to a final concentration 10 mg/mL lipids.

The proton influx assay was measured with the pH probe 9AA at the emission of 455 nm and the excitation of 326 nm in a microplate reader (PerkinElmer, USA) at room temperature. Add 10 μL prepared liposomes (liposomes only, RFVT2-WT or RFVT3-WT) to 90 μL of external buffer at pH 5.5 (20 mM MES, 100 mM NaCl) or pH 7.5 (20 mM HEPES, 100 mM NaCl), mixed well and added to a microplate to measure the fluorescence values. Riboflavin with a final concentration of 1 μM was added to the system, mixed and immediately measured. The final fluorescence signal was normalized to the respective fluorescence values at pH 7.5 in Prism 8.0.1 (GraphPad).

Riboflavin uptake assay was carried out by quantitative mass spectrometry analysis. Add 45 μL prepared liposomes (liposomes only, RFVT2-WT or RFVT3-WT) to 450 μL of external buffer at pH 5.5 or pH 7.5. The liposomes were mixed with 1 μM riboflavin-(dioxopyrimidine-$^{13}C4$, $^{15}N2$) and incubated for 10 min on ice. After removing excess substrate, the membrane-filtered liposomes were dissolved in 500 μL of 80% (v/v) methanol solvent and were placed at −80 °C for half an hour. After removing the filter membrane, the extraction solutions were transferred into a new brown tube for vacuum concentration and data collection by quantitative mass spectrometry analysis.

Cryo-EM sample preparation and data collection

Before grid preparation, 0.5 mM riboflavin was added to the purified samples, which were incubated on ice for 1 h. Aliquots of 3.0 μL of the samples were placed on glow-discharged holey carbon grids (Cu R1.2/1.3, 300-mesh, Quantifoil). Using a Vitrobot Mark IV (Thermo Scientific, USA), the grids loaded with samples were blotted for 3.0–4.5 s with filter papers and were plunge-frozen in liquid ethane cooled by liquid nitrogen with 100% humidity at 4 °C. The grids were inspected and cryo-EM data were acquired using a 300 kV Titan Krios G4 transmission electron microscope (Thermo Scientific, USA) equipped with a K3 direct detector (Gatan, USA) and a BioQuantum GIF energy filter (Gatan, USA) with a slit width of 10 eV. All movie stacks were automatically collected using the EPU v3.1 (Thermo Scientific, USA) at a magnification of 105,000 with a physical pixel size of 0.85 Å (super-resolution mode). The dose rate was set at 15 e/pix/s, and the exposure time is 2.89 s, yielding a total dose of 60 e/Å^2. Each movie contains 40 fractionated frames. The defocus range was set between −1.0 μm and −2.0 μm. A total of 4116 and 3477 movie stacks were collected for RFVT2 and RFVT3, respectively.

Cryo-EM data processing

For RFVT2, 4116 movie stacks were imported into RELION-3.1[53] and were motion-corrected, binned by twofold and dose-weighted using MotionCorr2 v1.6.3[54] in 5 × 5 patches. Defocus values of each summed micrograph were estimated using Gctf v1.3[55]. A total of 4108 micrographs with contrast transfer function (CTF) fitting resolution better than 4 Å were selected for particle picking. A total of 2,720,825 picked particles were binned by twofold and extracted in a box with a size of 128. The particles were imported into CryoSPARC v4.1.0[56] and two rounds of 2D classification were performed, resulting in 2,358,767 good particles. A small set of good 2D averages was subjected to ab initio reconstruction, generating an initial model for subsequent three rounds of Heterogeneous Refinement. A total of 341,051 selected particles were re-extracted in a box with a size of 256 and a pixel size of 0.85 Å. Then the particles were subjected to Non-uniform refinement, yielding a map at 4.01 Å. The particles were further subjected to local

3D classification with a focused mask covering the TMD region, resulting in 229,341 good particles which were polished in RELION-3.1. The polished particles were subjected to 2D and 3D classification, Non-uniform and Local Refinement. Finally, an EM map of RFVT2^{EM} was obtained at a resolution of 3.01 Å from 143,636 particles.

The RFVT3 data were processed similarly. In brief, 4,273,317 particles were auto-picked and extracted from 3434 micrographs. After two rounds of 2D classification in CryoSPARC, 1,274,836 good particles were subjected to ab initio reconstruction and three rounds of Heterogeneous Refinement. Then a refined map at 3.96 Å was generated from Non-uniform Refinement using 456,902 particles. Further 3D classification, particle polishing, skip-alignment 3D classification ($T = 30$; $K = 6$), Non-uniform Refinement and Local refinement were performed, yielding a final EM map of RFVT3^{EM} at a resolution of 3.29 Å using 99,741 particles. The detailed data processing flowcharts are presented in Supplementary Figs. 2 and 3.

Model building and refinement

The AlphaFold2 models of human RFVT2 (accession code: AF-Q9HAB3-F1) and RFVT3 (accession code: AF-Q9NQ40-F1) were manually fitted into the final EM maps of RFVT2^{EM} and RFVT3^{EM} using Chimera v1.15[57]. The TM helices were manually fitted into the corresponding densities and the rotamers of the side chains were corrected in COOT v0.9.2[58]. The corrected models were refined in Phenix v1.19[59]. The FSC curves of the refined models to their EM maps were calculated by Phenix.mtrage. The cryo-EM data collection and model refinement statistics are summarized in Supplementary Table 1.

All the figures were prepared with PyMOL v2.4.0 (Schrödinger, LLC), Prism v8.0.1 (GraphPad Software), and ChimeraX v1.1[60].

Molecular dynamics

Our molecular dynamics (MD) simulation studies involved two systems: the RFVT2 complexed with and without riboflavin in the outward-facing state, and the RFVT3 complexed with and without riboflavin in the inward-facing state. The cryo-EM structures were used as initial models. To support the protonation state configuration of the residues, PROPKA3 (version 3.4.0)[61] was used to empirically estimate the pKa values of the residues. ACE (acetyl) and NME (N-methylamide) were used to cap the C- and N-termini of the protein, respectively. The details of the configuration of MD simulation, including the force field preparation for the protein, DMPC lipids, and ligands, and controlling parameters, were consistent with our previous study[62].

For each system, three independent production runs were performed, each with a duration of 400 ns. No constraints were imposed on the ligand or protein during the MD simulations. The protein exhibited a stable backbone r.m.s.d. plot after 50 ns. The MM/GBSA[36] calculations were carried out on 350 frames ranging from 50 to 400 ns for each independent trajectory. The GROMACS2021 suite of programs was used for all the simulations[63].

Lastly, due to the presence of two ligands (central and upper riboflavin molecules) bound to RFVT2 in the cryo-EM structure, an additional system with the upper riboflavin molecule removed from the initial structure was also involved in the MD study. We observed that the MM/GBSA[36] binding free energy of the central riboflavin molecule showed a negligible increase of ~2 kcal/mol in the presence of the upper riboflavin molecule.

Reporting summary

Further information on research design is available in the Nature Portfolio Reporting Summary linked to this article.

Data availability

Data supporting the findings of this work are available from the corresponding author upon request. The coordinates and the cryo-EM density maps of human RFVT2 and RFVT3 generated in this study have been deposited in the Protein Data Bank (PDB) and the Electron Microscopy Data Bank (EMDB) under accession codes PDB: 8XSM, EMD-38622 and PDB: 8XSN, EMD-38623, respectively. Previously published data for cryo-EM structures of hENT1 and *Pf*ENT1 are available with PDB accession codes PDB: 6OB6 and PDB: 7WN0 respectively. The files relating to the MD simulations can be found at Figshare [https://doi.org/10.6084/m9.figshare.28713224.v1]. Source data are provided with this paper.

References

1. Powers, H. J. Riboflavin (vitamin B-2) and health. *Am. J. Clin. Nutr.* **77**, 1352–1360 (2003).
2. Joosten, V. & Van Berkel, W. J. Flavoenzymes. *Curr. Opin. Chem. Biol.* **11**, 195–202 (2007).
3. Barile, M. et al. Biosynthesis of flavin cofactors in man: implications in health and disease. *Curr. Pharm. Des.* **19**, 2649–2675 (2013).
4. Efsa Panel On Dietetic Products, N. et al. Dietary reference values for riboflavin. *Efsa J.* **15**, E04919 (2017).
5. Yonezawa, A., Masuda, S., Katsura, T. & Inui, K. Identification and functional characterization of a novel human and rat riboflavin transporter, RFT1. *Am. J. Physiol. Cell Physiol.* **295**, C632–C641 (2008).
6. Yao, Y. et al. Identification and comparative functional characterization of a new human riboflavin transporter HRFT3 expressed in the brain. *J. Nutr.* **140**, 1220–1226 (2010).
7. Yamamoto, S. et al. Identification and functional characterization of rat riboflavin transporter 2. *J. Biochem.* **145**, 437–443 (2009).
8. Barile, M., Giancaspero, T. A., Leone, P., Galluccio, M. & Indiveri, C. Riboflavin transport and metabolism in humans. *J. Inherit. Metab. Dis.* **39**, 545–557 (2016).
9. Jin, C. & Yonezawa, A. Recent advances in riboflavin transporter RFVT and its genetic disease. *Pharm. Ther.* **233**, 108023 (2022).
10. Yonezawa, A. & Inui, K. Novel riboflavin transporter family RFVT/SLC52: identification, nomenclature, functional characterization and genetic diseases of RFVT/SLC52. *Mol. Asp. Med.* **34**, 693–701 (2013).
11. Yoshimatsu, H. et al. Functional involvement of RFVT3/SLC52A3 in intestinal riboflavin absorption. *Am. J. Physiol. Gastrointest. Liver Physiol.* **306**, G102–G110 (2014).
12. Yao, Y. et al. Involvement of riboflavin transporter RFVT2/SLC52A2 in hepatic homeostasis of riboflavin in mice. *Eur. J. Pharm.* **714**, 281–287 (2013).
13. Ho, G. et al. Maternal riboflavin deficiency, resulting in transient neonatal-onset glutaric aciduria type 2, is caused by a microdeletion in the riboflavin transporter gene GPR172B. *Hum. Mutat.* **32**, E1976–E1984 (2011).
14. Mosegaard, S. et al. An intronic variation in SLC52A1 causes exon skipping and transient riboflavin-responsive multiple acyl-CoA dehydrogenation deficiency. *Mol. Genet. Metab.* **122**, 182–188 (2017).
15. Green, P. et al. Brown-Vialetto-Van Laere syndrome, a ponto-bulbar palsy with deafness, is caused by mutations in c20orf54. *Am. J. Hum. Genet.* **86**, 485–489 (2010).
16. Bosch, A. M. et al. Brown-Vialetto-Van Laere and Fazio Londe syndrome is associated with a riboflavin transporter defect mimicking mild MADD: a new inborn error of metabolism with potential treatment. *J. Inherit. Metab. Dis.* **34**, 159–164 (2011).
17. Jaeger, B. & Bosch, A. M. Clinical presentation and outcome of riboflavin transporter deficiency: mini review after five years of experience. *J. Inherit. Metab. Dis.* **39**, 559–564 (2016).
18. Bartmann, L. et al. Evaluation of riboflavin transporters as targets for drug delivery and theranostics. *Front. Pharm.* **10**, 79 (2019).
19. Tutino, V. et al. The expression of riboflavin transporters in human colorectal cancer. *Anticancer Res.* **38**, 2659–2667 (2018).
20. Jiang, X. R. et al. Rft2 is overexpressed in esophageal squamous cell carcinoma and promotes tumorigenesis by sustaining cell

proliferation and protecting against cell death. *Cancer Lett.* **353**, 78–86 (2014).
21. Darguzyte, M., Drude, N., Lammers, T. & Kiessling, F. Riboflavin-targeted drug delivery. *Cancers* https://doi.org/10.3390/Cancers12020295 (2020).
22. Gutierrez-Preciado, A. et al. Extensive identification of bacterial riboflavin transporters and their distribution across bacterial species. *PLoS ONE* **10**, E0126124 (2015).
23. Reihl, P. & Stolz, J. The monocarboxylate transporter homolog Mch5p catalyzes riboflavin (vitamin B2) uptake in *Saccharomyces cerevisiae*. *J. Biol. Chem.* **280**, 39809–39817 (2005).
24. Zhang, P., Wang, J. & Shi, Y. Structure and mechanism of the S component of a bacterial ECF transporter. *Nature* **468**, 717–720 (2010).
25. Fujimura, M. et al. Functional characteristics of the human ortholog of riboflavin transporter 2 and riboflavin-responsive expression of its rat ortholog in the small intestine indicate its involvement in riboflavin absorption. *J. Nutr.* **140**, 1722–1727 (2010).
26. Jin, C. et al. Riboflavin transporters RFVT/SLC52A mediate translocation of riboflavin, rather than FMN or FAD, across plasma membrane. *Biol. Pharm. Bull.* **40**, 1990–1995 (2017).
27. Wu, D. et al. Transport and inhibition mechanisms of human VMAT2. *Nature* https://doi.org/10.1038/S41586-023-06926-4 (2023).
28. Yan, N. Structural biology of the major facilitator superfamily transporters. *Annu. Rev. Biophys.* **44**, 257–283 (2015).
29. Drew, D., North, R. A., Nagarathinam, K. & Tanabe, M. Structures and general transport mechanisms by the major facilitator superfamily (MFS). *Chem. Rev.* **121**, 5289–5335 (2021).
30. Wright, N. J. & Lee, S. Y. Structures of human ENT1 in complex with adenosine reuptake inhibitors. *Nat. Struct. Mol. Biol.* **26**, 599–606 (2019).
31. Wang, C. et al. Structural basis of the substrate recognition and inhibition mechanism of *Plasmodium falciparum* nucleoside transporter PFENT1. *Nat. Commun.* **14**, 1727 (2023).
32. Saier, M. H. Jr. Transport protein evolution deduced from analysis of sequence, topology and structure. *Curr. Opin. Struct. Biol.* **38**, 9–17 (2016).
33. Ferrada, E. & Superti-Furga, G. A structure and evolutionary-based classification of solute carriers. *Iscience* **25**, 105096 (2022).
34. Qureshi, A. A. et al. The molecular basis for sugar import in malaria parasites. *Nature* **578**, 321–325 (2020).
35. Yang, D. & Gouaux, E. Illumination of serotonin transporter mechanism and role of the allosteric site. *Sci. Adv.* **7**, Eabl3857 (2021).
36. Genheden, S. & Ryde, U. The MM/PBSA and MM/GBSA methods to estimate ligand-binding affinities. *Expert Opin. Drug Discov.* **10**, 449–461 (2015).
37. Grzesiek, S., Otto, H. & Dencher, N. A. Delta Ph-induced fluorescence quenching of 9-aminoacridine in lipid vesicles is due to excimer formation at the membrane. *Biophys. J.* **55**, 1101–1109 (1989).
38. Drew, D. & Boudker, O. Ion and lipid orchestration of secondary active transport. *Nature* **626**, 963–974 (2024).
39. Zhang, X. C., Zhao, Y., Heng, J. & Jiang, D. Energy coupling mechanisms of MFS transporters. *Protein Sci.* **24**, 1560–1579 (2015).
40. Solcan, N. et al. Alternating access mechanism in the pot family of oligopeptide transporters. *EMBO J.* **31**, 3411–3421 (2012).
41. Parker, J. L. et al. Structural basis of antifolate recognition and transport by PCFT. *Nature* **595**, 130–134 (2021).
42. Parker, J. L. & Newstead, S. Molecular basis of nitrate uptake by the plant nitrate transporter NRT1.1. *Nature* **507**, 68–72 (2014).
43. Yaffe, D., Forrest, L. R. & Schuldiner, S. The ins and outs of vesicular monoamine transporters. *J. Gen. Physiol.* **150**, 671–682 (2018).
44. Karpowich, N. K., Song, J. & Wang, D. N. An aromatic cap seals the substrate binding site in an ECF-type S subunit for riboflavin. *J. Mol. Biol.* **428**, 3118–3130 (2016).
45. Wright, N. J. et al. Methotrexate recognition by the human reduced folate carrier SLC19A1. *Nature* **609**, 1056–1062 (2022).
46. Pidathala, S. et al. Mechanisms of neurotransmitter transport and drug inhibition in human VMAT2. *Nature* **623**, 1086–1092 (2023).
47. Niu, Y. et al. Structural basis of inhibition of the human SGLT2-MAP17 glucose transporter. *Nature* **601**, 280–284 (2022).
48. Wang, Y. et al. Transport and inhibition mechanism for VMAT2-mediated synaptic vesicle loading of monoamines. *Cell Res.* https://doi.org/10.1038/S41422-023-00906-Z (2024).
49. Zhang, K., Wu, H., Hoppe, N., Manglik, A. & Cheng, Y. Fusion protein strategies for cryo-EM study of G protein-coupled receptors. *Nat. Commun.* **13**, 4366 (2022).
50. Xia, Z. et al. Structural insights into glucose-6-phosphate recognition and hydrolysis by human G6PC1. *Proc. Natl. Acad. Sci. USA* **122**, E2418316122 (2025).
51. Wu, D., Zhao, Y. & Jiang, D. Structural insights into substrate transport and drug inhibition of the human vesicular monoamine transporter 2 (VMAT2). *FEBS J.* https://doi.org/10.1111/Febs.70003 (2025).
52. Kuang, W. et al. SLC22A14 is a mitochondrial riboflavin transporter required for sperm oxidative phosphorylation and male fertility. *Cell Rep.* **35**, 109025 (2021).
53. Zivanov, J. et al. New tools for automated high-resolution cryo-EM structure determination in RELION-3. *eLife* https://doi.org/10.7554/Elife.42166 (2018).
54. Zheng, S. Q. et al. MotionCor2: anisotropic correction of beam-induced motion for improved cryo-electron microscopy. *Nat. Methods* **14**, 331–332 (2017).
55. Zhang, K. Gctf: real-time CTF determination and correction. *J. Struct. Biol.* **193**, 1–12 (2016).
56. Punjani, A., Rubinstein, J. L., Fleet, D. J. & Brubaker, M. A. Cryosparc: algorithms for rapid unsupervised cryo-EM structure determination. *Nat. Methods* **14**, 290–296 (2017).
57. Pettersen, E. F. et al. UCSF Chimera–a visualization system for exploratory research and analysis. *J. Comput Chem.* **25**, 1605–1612 (2004).
58. Emsley, P. & Cowtan, K. Coot: model-building tools for molecular graphics. *Acta Crystallogr. D. Biol. Crystallogr.* **60**, 2126–2132 (2004).
59. Adams, P. D. et al. Phenix: a comprehensive Python-based system for macromolecular structure solution. *Acta Crystallogr. D. Biol. Crystallogr.* **66**, 213–221 (2010).
60. Pettersen, E. F. et al. Ucsf Chimerax: structure visualization for researchers, educators, and developers. *Protein Sci.* **30**, 70–82 (2021).
61. Olsson, M. H., Sondergaard, C. R., Rostkowski, M. & Jensen, J. H. PROPKA3: consistent treatment of internal and surface residues in empirical pka predictions. *J. Chem. Theory Comput.* **7**, 525–537 (2011).
62. Li, Y. et al. Structure of human Na(V)1.6 channel reveals Na(+) selectivity and pore blockade by 4,9-anhydro-tetrodotoxin. *Nat. Commun.* **14**, 1030 (2023).
63. Van Der Spoel, D. et al. Gromacs: fast, flexible, and free. *J. Comput Chem.* **26**, 1701–1718 (2005).

Acknowledgements

We thank B. Xu at the Cryo-EM Center of School of Advanced Agricultural Sciences of Peking University and D. Sun at the SM10 Cryo-EM Facility Center at the Institute of Physics, Chinese Academy of Sciences & Beijing Branch of Songshan Lake Materials Laboratory for support in cryo-EM sample preparation and data collection. We thank Ms. Wei Fan for her research assistance service. This work is funded by the National Natural Science Foundation of China (grant nos. 32271272 and T2221001 to D.J., 32130048 and 92157301 to L. Chen, U23A20143 and 32070031 to J.J.), the Beijing Municipal Science and Technology Commission (Z241100007724005 to B.H.), and the Ministry of Science and Technology of China National Key R&D Programs (2022YFA0806503 to L. Chen).

Author contributions

D.J. conceived and designed the experiments. K.W. made all the constructs and prepared the samples for cryo-EM analysis. D.W., H.C., and J.Z. collected the cryo-EM data. H.C. and K.W. processed the data, built and refined the models. L. Cheng., X.H., Y.Z. and Y.Y. performed the riboflavin transport assays. B.H. and F.Z. performed the MD simulation studies. K.W. and H.C. prepared all figures. J.J., L. Chen, and D.J. analyzed and interpreted the results. D.J. wrote the paper, and all the authors reviewed and revised the paper.

Competing interests

The authors declare no competing interests.

Additional information

Supplementary information The online version contains supplementary material available at https://doi.org/10.1038/s41467-025-59255-7.

Correspondence and requests for materials should be addressed to Juquan Jiang, Ligong Chen or Daohua Jiang.

Peer review information *Nature Communications* thanks the anonymous reviewer(s) for their contribution to the peer review of this work. A peer review file is available.